

Correlation of Electronic Structure with Catalytic Activity: H₂–D₂ Exchange across Cu_xPd_{1-x} Composition Space

G. Gumuslu,[†] P. Kondratyuk,[†] J. R. Boes,[†] B. Morreale,^{†,‡} J. B. Miller,^{†,‡} J. R. Kitchin,^{†,‡} and A. J. Gellman^{*,†,‡}

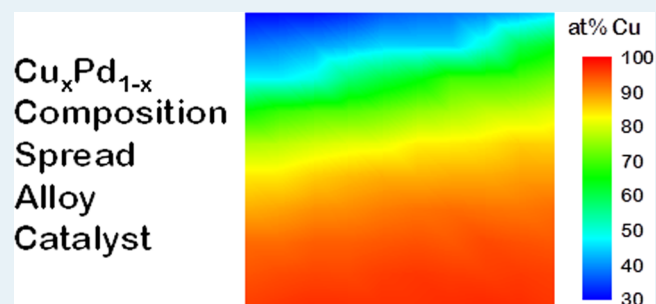
[†]Department of Chemical Engineering, Carnegie Mellon University, 5000 Forbes Avenue, Pittsburgh, Pennsylvania 15213, United States

[‡]DOE National Energy Technology Laboratory, P. O. Box 10940, Pittsburgh, Pennsylvania 15236, United States

S Supporting Information

ABSTRACT: The relationship between alloy catalyst activity and valence band electronic structure has been investigated experimentally across a broad, continuous span of Cu_xPd_{1-x} composition space. Cu_xPd_{1-x} composition spread alloy films (CSAFs) were used as catalyst libraries with a 100 channel microreactor to measure the H₂–D₂ exchange kinetics over a temperature range of 333–593 K at 100 discrete Cu_xPd_{1-x} compositions spanning the range $x = 0.30$ – 0.97 . The H₂–D₂ exchange activity exhibits a monotonic decrease over the composition range $x = 0.30$ – 0.97 . A steady state, microkinetic model was used to estimate the energy barriers to dissociative H₂ adsorption, $\Delta E_{\text{ads}}^{\ddagger}$, and recombinative H₂ desorption, $\Delta E_{\text{des}}^{\ddagger}$, as functions of alloy composition, x . Their values fall in the ranges $\Delta E_{\text{ads}}^{\ddagger}(x) = 0.15$ to 0.45 eV and $\Delta E_{\text{des}}^{\ddagger}(x) = 0.55$ – 0.65 eV. Spatially resolved UV photoemission spectra were obtained from the Cu_xPd_{1-x} CSAF and used to estimate the average energy of the filled states of the valence band as a function of alloy composition, $\epsilon_v(x)$. The energy of the v-band center shifted monotonically from $\epsilon_v = -3.3$ to -3.9 eV across the composition range $x = 0.30$ – 0.97 . This monotonic shift and its magnitude were corroborated by DFT calculations. The correlation of $\Delta E_{\text{ads}}^{\ddagger}(x)$ with $\epsilon_v(x)$ across alloy composition space yields $\Delta E_{\text{ads}}^{\ddagger}(\epsilon_v)$ which decreases as the v-band energy shifts toward the Fermi level.

KEYWORDS: hydrogen, palladium, alloys, electronic structure, catalysis, membranes, adsorption



1. INTRODUCTION

Multicomponent metal alloys are used as catalysts for many processes because alloys often display catalytic properties superior to those of their pure elemental components.^{1,2} The activity and selectivity of alloy catalysts can be controlled and optimized by changing either the alloy components (elements) or the alloy composition (elemental fraction). These changes influence catalytic activity by modifying the electronic structure and atomic surface structure of the alloy.^{3,4} A deep understanding of the relationships among alloy composition, atomic structure, electronic structure, and catalytic reactivity requires some means of measuring or modeling these alloy characteristics and properties across composition space. This poses an extremely difficult challenge to both computational theory and experiment because composition space is multidimensional and continuous, requiring the preparation of catalyst samples (or computational models) in numbers that increase exponentially with the number of components in the alloy.

For the most part, activity–structure–composition relationships for multicomponent alloy catalysts have been developed using computational electronic structure methods. Adsorbed species interact with d-band valence electrons of metal

surfaces.^{3,5,6} Many computational studies of alloy catalysts of varying composition have focused on the influence of the d-band electronic structure on catalytic activity by developing simple relationships between characteristics of the d-band energy distribution and the activation barriers to elementary steps in a catalytic reaction mechanism. These studies have shown that the mean energy of the d-band, ϵ_d , is an important parameter in determining the catalytic activity of metals.^{2,3,5–9} When an adsorbate electronic state interacts with the d electrons of the metal, a splitting into bonding and antibonding states occurs. The energies of the bonding and antibonding states determine the strength of chemisorption and, thus, the reactivity of the surface. If the antibonding state is above the Fermi level and unoccupied, the bond with the surface is strong. If the antibonding level is below the Fermi level and occupied, the bond with the surface is weak. As a result, the strength of adsorbate bonding to the surface tends to increase as the energy of the d-band shifts toward the Fermi level.⁵

Received: October 14, 2014

Revised: February 26, 2015

Published: April 7, 2015

Experimental demonstrations of relationships among alloy composition, electronic structure, and catalytic activity require preparation and characterization of a large set of catalysts whose individual compositions sample composition space with the requisite resolution. This approach is time-consuming and limits the feasible size of the sample set. This limited sampling of composition space constrains the level of detail at which relationships between alloy characteristics and catalytic activity can be defined. Progress has been limited by the labor-intensive nature of the processes needed to prepare and characterize large numbers of catalyst samples.¹⁰ To address this problem, we have developed a high-throughput methodology for determination of alloy characteristics and catalytic properties by experiments that can span the entire composition space of binary (A_xB_{1-x}) or ternary ($A_xB_yC_{1-x-y}$) alloys. The approach is based on the use of composition spread alloy films (CSAFs), alloy catalyst libraries that include all possible compositions of an alloy in the form of a thin film deposited on a single substrate.^{11,12}

The CSAF concept for acceleration of alloy composition–property studies dates back to the 1950s,¹³ however, its practical implementation was limited at that time by lack of the instrumented data acquisition and automated data analysis tools needed to take full advantage of the potential of CSAFs. Over the past two decades, these capabilities have developed rapidly, and the full potential of CSAFs is now readily attainable.^{13,14} There are a variety of methods for preparation of CSAFs, including sputtering, electron-beam evaporation, and pulsed laser deposition.^{15–18} These elemental deposition sources can be combined with various means for establishing a flux gradient across the substrate to generate the composition spread.^{16,19–23} Previously, CSAFs have been used as high-throughput materials libraries for characterization of phase diagrams and bulk alloy properties, such as dielectric constant, magnetic moment, optical properties, etc.^{15,17,18,23–28}

High-throughput methods have had increasing impact in studies of catalysis because they enable rapid, systematic characterization of large numbers of catalysts.²⁹ There have been a number of designs reported for high-throughput catalyst libraries and for multichannel reaction systems to accelerate the screening of catalytic properties, such as selectivity and reactivity across these libraries to discover and optimize new catalysts.^{30–32} Although CSAFs have not been applied in studies of heterogeneous gas–solid catalysis, they have been used successfully by Hayden et al. in a number of studies of electrocatalysis.^{33–36} The advantage of the CSAF catalyst libraries is that they allow detailed study of catalytic activity across entire binary and ternary alloy composition spaces and on libraries that are amenable to characterization using a wide range of surface and materials analysis methods. They do, however, require the development of a specialized, high-throughput reactor that is compatible with the compact size, ~ 1 cm², area of the CSAFs.³⁷

Herein, we describe a high-throughput study of catalytic H₂–D₂ exchange kinetics on Cu_xPd_{1-x} alloy catalysts that span a continuous range of composition space ($x = 0.30–0.97$). H₂–D₂ exchange is an ideal test reaction for demonstration of our methodology because its kinetics, at least for the simplest possible mechanism, can be parametrized in terms of two rate constants—one for dissociative adsorption, $k_{\text{ads}}^{\text{H}_2}$, and one for recombinative desorption, $k_{\text{des}}^{\text{H}_2}$ —of H₂. Measurement of these rate constants over a range of temperatures has been used to estimate the barriers to dissociative H₂ adsorption, $\Delta E_{\text{ads}}^{\ddagger}$, and

recombinative H₂ desorption, $\Delta E_{\text{des}}^{\ddagger}$, across Cu_xPd_{1-x} alloy composition space. The adsorption and desorption of H₂ from Pd alloy surfaces is relevant to the application of Pd alloys in catalytic hydrogenation and as H₂ purification membranes.^{38–47}

We have previously measured the steady state kinetics of H₂–D₂ exchange over Pd, Cu_{0.30}Pd_{0.70}, Cu_{0.53}Pd_{0.47}, and Cu foils in a flow reactor at atmospheric pressure and over the temperature range 200–900 K.⁴⁸ The Cu_{0.53}Pd_{0.47} alloy can be prepared in either a FCC or B2 phase, depending upon thermal treatment, and pure Pd can exist in α -PdH or β -PdH phases, depending upon hydrogen pressure.^{49,50} The influence of Cu–Pd composition on H₂–D₂ exchange activity is somewhat surprising: FCC-Cu_{0.53}Pd_{0.47} > Cu_{0.30}Pd_{0.70} > B2-Cu_{0.53}Pd_{0.47} > β -PdH \approx α -PdH \gg Cu. In other words, the addition of Cu to Pd increases its overall activity for H₂–D₂ exchange. The other interesting observation is that for Cu_{0.53}Pd_{0.47}, the activity of the FCC phase is much higher than that of the thermodynamically stable B2 phase. Microkinetic analysis was used to estimate $\Delta E_{\text{ads}}^{\ddagger}$ and $\Delta E_{\text{des}}^{\ddagger}$ on each of these six Cu–Pd catalysts. The results of that work serve to benchmark the study described herein. In this work, the H₂ adsorption and desorption barriers have been determined for Cu_xPd_{1-x} ($x = 0.30–0.97$) under conditions similar to those used with the single composition foil catalysts. The unique feature of this work is that the barriers have been measured across a wide, continuous region of alloy composition space to yield $\Delta E_{\text{ads}}^{\ddagger}(x)$ and $\Delta E_{\text{des}}^{\ddagger}(x)$.

In addition to characterization of the catalytic activities of the Cu_xPd_{1-x} CSAF, its electronic structure has been measured across composition space using UV photoemission spectroscopy (UPS). UPS was used to estimate the average energy of the filled states of the valence band (*s*-, *p*-, and *d*-bands) across composition space, $\epsilon_v(x)$, and to show that the *v*-band shifts toward the Fermi level as the Cu fraction decreases. The measured *v*-band energy has been used as an experimental proxy for the *d*-band energy calculated using DFT. The key point is that $\Delta E_{\text{ads}}^{\ddagger}(x)$, and $\epsilon_v(x)$ can be correlated across the same region of composition space to give $\Delta E_{\text{ads}}^{\ddagger}(\epsilon_v)$. We find that $\Delta E_{\text{ads}}^{\ddagger}$ decreases as ϵ_v increases, but not linearly. This represents the most comprehensive attempt to date to measure experimentally the type of relationship between electronic structure and reaction barrier that is predicted by many computational modeling studies of catalysis.^{5,6,9,51,52} The primary intent of this paper is to demonstrate a general experimental methodology for correlating the kinetic parameters of catalytic reactions with physical characteristics of catalytic surfaces across continuous regions of alloy catalyst composition space. This is a fairly general methodology that should be applicable to a wide range of alloy-catalyzed reactions at gas–solid surfaces.

2. METHODS

2.1. CSAF Preparation. Cu_xPd_{1-x} CSAFs were prepared by evaporative deposition of Pd and Cu onto 14 × 14 × 2 mm³ Mo substrates (Valley Design Corp.) using an offset-filament tool that we have described previously.⁵³ In this tool, line sources consisting of Cu or Pd wires embedded in heating elements were positioned on opposite sides of the substrate with an offset from its edges. The source–substrate geometry, the source operating temperature, and the deposition time determine the range of the spread (i.e., the range of x), the CSAF thickness (~ 100 nm in this work), and its orientation on the substrate surface. We have used a Mo substrate to minimize the potential for substrate interdiffusion with the CSAF during

heating to 800 K.^{4,11,54,55} Mo substrates were cleaned with acetone before being placed into the deposition chamber. CSAFs were deposited and then annealed (800 K for 1 h) under ultrahigh vacuum (UHV) conditions. We previously characterized the bulk structure and the surface segregation properties of Cu_xPd_{1-x} CSAFs prepared using these methods.¹¹ Under UHV conditions, there is a tendency for Cu to segregate to the uppermost atomic layer. More importantly, Cu_xPd_{1-x} CSAFs exhibit the FCC and B2 phases over the same composition range as observed in the bulk.⁵⁰

2.2. Characterization of CSAF Composition and Electronic Structure. Annealed CSAFs were characterized by obtaining spatially resolved UPS and X-ray photoelectron spectra (XPS) in a ThetaProbe surface analysis system (ThermoFisher Scientific Inc.). UPS spectra were obtained with the CSAF at 300 K using He I photoemission (21.2 eV). A 20 cm long collimating tube was mounted on the UV source with 500 μm apertures on both ends, creating a spot size of ~600 μm on the CSAF. The current of photoelectrons with kinetic energies in the range 0–25 eV was measured using the ThetaProbe analyzer with a pass energy of 20 eV. XPS was used to determine the near-surface composition at discrete locations on the CSAF. XPS spectra were obtained with the CSAF at 300 K using a monochromatic Al K_α X-ray source (1486 eV) with a spot size of 200 μm and analyzer pass energy of 40 eV. The fractional atomic compositions at each point were extracted by the Avantage Data System software. This software has a library of peak positions and relative intensities for pure metals. After performing a background subtraction using principal component analysis reconstruction, the software library was used to identify the components and their concentrations from measured spectra of the Pd 3d_{5/2} and Cu 2p_{3/2} peaks.

2.3. Measurement of H₂–D₂ Exchange Kinetics. A multichannel microreactor array was used to measure the kinetics of the H₂–D₂ exchange reaction at 100 different points (compositions) on the Cu_xPd_{1-x} CSAF and under a variety of different flow and temperature conditions. The details of the microreactor array and its operation have been described elsewhere.³⁷ Briefly, the microreactor array was composed of 100 inlet–outlet channel pairs, each pair defining a reaction volume with a footprint of 700 × 900 μm², in a 10 × 10 array across the CSAF surface. A perfluoroelastomer gasket (Dupont Kalrez 7075) with 100 rectangular holes (700 × 900 μm²) was sandwiched between the CSAF and the microreactor array to create 100 isolated reaction volumes connecting the inlet–outlet pairs. Flow of two different gases through adjacent reactors and mass spectrometric analysis of the gases in their outlets was used to demonstrate that there is no cross-talk between reactors.³⁷ The flow rates of H₂, D₂ and Ar (all at 99.999%, Valley National Gases) were controlled by mass flow controllers (Aalborg GFC 17), and the reactor system distributed the gases equally among all 100 inlet channels leading to the Cu_xPd_{1-x} CSAF surface. The back side of the Mo substrate was in direct thermal contact with an electric heater used to control the temperature in the range 300–600 K. The product gas streams from the 100 microreactors were isolated from one another and delivered by 100 glass capillary tubes to an automated, home-built gas sampler.³⁷ The sampler allowed sequential collection of the product gas streams by a glass capillary leading to a mass spectrometer (Stanford Research Systems, RGA 200), which was used for analysis of the product gas composition.

The Cu_xPd_{1-x} CSAF surface was conditioned in a total flow of 30 mL/min H₂ at 300 K for 3 h before starting H₂–D₂ exchange measurements. Between experiments, the CSAF surface was left at 300 K in contact with H₂ at a total flow of 5 mL/min. After surface treatment, a H₂/D₂/Ar gas mixture was introduced to the microreactor. H₂–D₂ exchange was catalyzed by the Cu_xPd_{1-x} CSAF over the temperature range $T = 333$ –593 K using three H₂/D₂/Ar flow conditions at atmospheric pressure (Table 1). The temperature was

Table 1. Flow Rates of H₂, D₂, and Ar at $P_{Tot} = 1$ atm for the Different Inlet Gas Mixtures^a

| inlet gas condition | $F_{H_2}^{in}$ (mL/min) | $F_{D_2}^{in}$ (mL/min) | F_{Ar}^{in} (mL/min) | $F_{tot}/channel$ (mL/min) | $P_{H_2} = P_{D_2}$ (atm) |
|---|-------------------------|-------------------------|------------------------|----------------------------|---------------------------|
| 15 H ₂ / 15 D ₂ | 15 | 15 | 0 | 0.03 | 0.5 |
| 25 H ₂ / 25 D ₂ | 25 | 25 | 0 | 0.05 | 0.5 |
| 15 H ₂ / 15 D ₂ / 30 Ar | 15 | 15 | 30 | 0.06 | 0.25 |

^aThe actual inlet flow to each microreactor is given by the flow rate divided by 100.

increased in 20 K increments, and the reaction was allowed to reach a steady state by waiting for 6 min at each temperature before beginning the analysis of the product gas streams.

The H₂ conversion in each reaction volume was calculated by assuming that the background-subtracted mass spectrometer signals at $m/z = 2, 3$, and 4 amu were proportional to the flow rates of H₂, HD, and D₂ but with different sensitivity factors. For background subtraction, we considered the fragmentation pattern of D₂ at $m/z = 2$ and the signal occurring at $m/z = 3$ due to minor H₂–HD impurity in D₂. Using the signals at $m/z = 2$ and 3, the H₂ conversion, X , in each channel was calculated using

$$\frac{S_3}{S_2} = \frac{Z_{3,HD} F_{HD}^{out}}{Z_{2,H_2} F_{H_2}^{out}} = \frac{Z_{3,HD}}{Z_{2,H_2}} \frac{2XF_{H_2}^{in}}{F_{H_2}^{in}(1-X)} \quad (1)$$

where S_n is the signal at $m/z = n$, $Z_{n,i}$ is the sensitivity factor for species i at $m/z = n$, and F_i is the molar flow rate of species i . The ratio of the sensitivity factors was determined to be 0.75 by calibrations under conditions that achieved equilibrium conversion. For calibration, we replicated the H₂–D₂ experiment on Pd foil as reported by O'Brien et al.⁴⁸ The surface area of Pd was ~19 cm², and the temperature range was 473–773 K. Signal intensities at $m/z = 2, 3$, and 4 were independent of temperatures above 573 K, which was assumed to indicate the establishment of equilibrium for the reaction. Note that equilibrium conversion results in partial pressures of H₂, HD, and D₂ that are related by⁵⁶

$$\frac{P_{HD}^2}{P_{H_2}P_{D_2}} = 4.16 \times \exp\left(\frac{-77.7}{T}\right) \quad (2)$$

and does not result in the complete consumption of H₂ and D₂.

2.4. Computational Methods. Density functional theory (DFT) was used to calculate the valence band electronic structure of Cu–Pd alloys and, in particular, the valence band energies for comparison with those estimated from UPS. Bulk alloy models were constructed at compositions $x = 0.0, 0.167, 0.25, 0.375, 0.5, 0.625, 0.75, 0.875$, and 1.0 on the basis of predicted ground state configurations from previous work.^{57,58}

All calculations were performed using the Vienna ab initio simulation package (VASP)^{59,60} with the Perdew–Burke–Ernzerhof generalized gradient approximation^{61,62} exchange–correlation functional. Core electrons were described using projector augmented wave functions.^{63,64} k -Points were represented using Monkhorst–Pack grids⁶⁵ with 8000 k -points per reciprocal atom. A planewave cutoff energy of 400 eV was used. The densities of states (DOS) was computed for each of these configurations and for pure Cu and Pd. The tetrahedron method with Blöchl corrections was used with a smearing parameter of 0.1 eV. Ionic relaxation was performed, and the forces in all structures were found to be less than 0.07 eV/Å. Atom-projected densities of states were computed using the standard methods in VASP. We used Wigner–Seitz radii of 1.5 and 3.0 Å for comparison. Detailed information about each of the bulk structures used in this study can be found in the Supporting Information file.

3. RESULTS

3.1. Characterization of CSAF Composition. The surface composition of the $\text{Cu}_x\text{Pd}_{1-x}$ CSAF was mapped using spatially resolved XPS. Although the CSAF is deposited onto a $14 \times 14 \text{ mm}^2$ Mo substrate, the region of interest is the $10 \times 10 \text{ mm}^2$ region spanned by the 10×10 array of microreactors. Because the microreactor array is aligned with the edges of the Mo substrate, we deposited the CSAF with its main axis “tilted” relative to the substrate edge to have the 100 microreactors sample 100 different $\text{Cu}_x\text{Pd}_{1-x}$ compositions. The tilt is easily observable in Figure 1 by the orientation of the

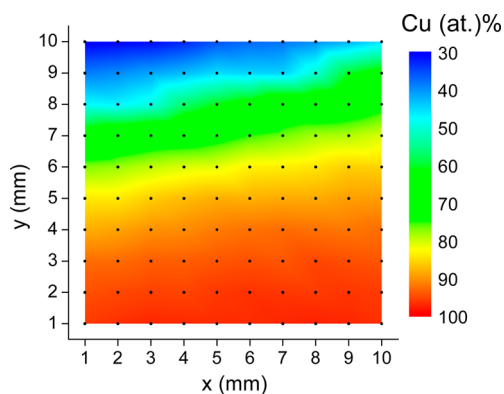


Figure 1. $\text{Cu}_x\text{Pd}_{1-x}$ composition as determined by XPS (Cu $2p_{3/2}$ and Pd $3d_{5/2}$) with respect to position across the CSAF surface. Black dots represent the positions of the measurement points. The concentration profile is intentionally tilted with respect to the square substrate.

iso-composition lines of constant color. In the region sampled by the microreactor array, the $\text{Cu}_x\text{Pd}_{1-x}$ CSAF spanned the composition range $x = 0.30$ – 0.97 . One of the inherent limitations of the offset filament method used to create the CSAFs for this study is that the resulting CSAFs cannot span compositions from pure Cu to pure Pd.⁵³ A more recently developed, but more complex, CSAF deposition tool based on the use of shadow masks circumvents this limitation and allows preparation of CSAFs that span all of the binary or ternary alloy composition space.⁶⁶

3.2. Characterization of CSAF Electronic Structure.

The valence band electronic structure of the $\text{Cu}_x\text{Pd}_{1-x}$ CSAF was mapped using UPS to measure the energy distribution of the filled valence band levels, that is, the density of filled states,

at points spanning the $\text{Cu}_x\text{Pd}_{1-x}$ composition space. Figure 2 shows the background-subtracted UP spectra obtained at 100

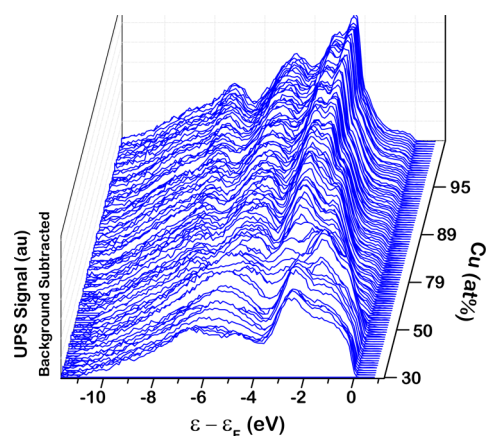


Figure 2. Background-subtracted UP spectra of 100 different $\text{Cu}_x\text{Pd}_{1-x}$ alloy compositions spanning the range $x = 0.30$ – 0.97 . These reveal the density of filled states versus energy with respect to the Fermi level. As the Cu composition decreases, there is a continuous shift of the filled valence band toward the Fermi level.

different $\text{Cu}_x\text{Pd}_{1-x}$ compositions. The low-energy secondary electron contributions to the UPS spectra were removed using the background-subtraction method described by Li et al.⁶⁷ In Figure 2, the Fermi level is located at zero on the energy scale, and it is fairly clear that the density of states shifts toward the Fermi level as the Cu content of the alloy, x , decreases. In this work, we have used the mean energy of the filled levels in the valence band, ε_v , determined from UP spectra as a proxy for the d-band center often calculated using DFT. To estimate the energy of the v -band center as described by Mun et al., we used the weighted average of the occupied states obtained from the intensity of the background-subtracted UP spectra of $\text{Cu}_x\text{Pd}_{1-x}$.⁶⁸ The v -band centers of the alloys were calculated using the equation

$$\varepsilon_v = \frac{\int N(\varepsilon) \varepsilon d\varepsilon}{\int N(\varepsilon) d\varepsilon} \quad (3)$$

where ε is the energy relative to the Fermi level and ε_v is the energy of the v -band center. $N(\varepsilon)$ is the density of filled states at the energy, ε , taken to be proportional to the intensity of the UP spectrum. Integration was performed over the range -7 to 0 eV because the changes in features of the spectra, that is, the peak heights or locations, with Cu concentration were significant only over this energy range. It should be noted that the UP spectra probe the density of filled states only, not the empty states. However, the Cu d-band is full, and that of Pd contains nine electrons; the valence band in CuPd alloys is dominated by filled states, and thus, the value of ε_v , determined from the UP spectra through eq 3 only slightly underestimates that of the entire valence band. Furthermore, because the sp-band has only two electrons and is fairly flat, it does not shift significantly with composition. As a result, the sp-band contributes a roughly constant offset between the v -band energy measured using UPS and the d-band calculated using DFT.

The energy of the $\text{Cu}_x\text{Pd}_{1-x}$ v -band center versus alloy composition is shown in Figure 3 for 100 different compositions. As the Cu content decreases, the v -band center

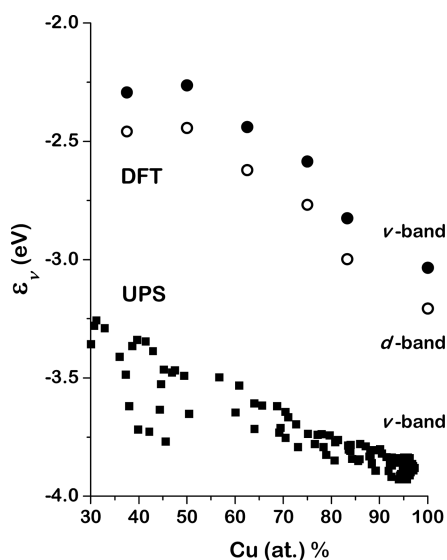


Figure 3. (■) UPS-derived average energy of the filled v-band relative to the Fermi level, ϵ_v , of a $\text{Cu}_x\text{Pd}_{1-x}$ alloy CSAF versus Cu composition, x . DFT estimates of the average energy of the filled d-band (○) and the average energy of the filled v-band total density of states (●). As the Cu composition decreases, the v-band shifts toward the Fermi level.

shifts toward the Fermi level, in accordance with observations from Figure 2. This result represents the first experimental demonstration of a correlation between alloy composition and the energy of its v-band center measured across a wide range of composition space. Existing data in the literature are limited to estimates of ϵ_d for pure Pd and Cu, most of which are derived from electronic structure calculations. The range of d-band energies reported for Cu is $\epsilon_d = -3.6$ to -2.53 eV and for Pd is $\epsilon_d = -2.2$ to -1.8 eV.^{6,8,9,52,69–74} The observed increase in ϵ_v with decreasing x is consistent with the reported d-band energies of pure Cu and Pd. The value of the v-band energy for Cu (at $x = 0.97$ on the CSAF) is estimated at $\epsilon_v = -3.9$ eV from the spectra in Figure 2. That of $\text{Cu}_{0.30}\text{Pd}_{0.70}$ is $\epsilon_v = -3.3$ eV, and the trend in Figure 3 suggests that the v-band energy of pure Pd is $\epsilon_v = -3.0$ eV.

Also plotted in Figure 3 are the valence band energies determined for Cu–Pd alloys using DFT calculations. These were calculated for the filled portion of the d-band and the filled portion of the total density of states (DOS). The key

point to be made is that the DFT-predicted shift in the energy of the filled portion of the total DOS mimics that observed experimentally from the UP spectra. Although there is an offset of ~ 0.8 eV between the DFT-predicted values of ϵ_v and those estimated from the UP spectra, the slopes of the two as functions of Cu composition are comparable. The offset in the absolute magnitudes of the valence band energies from DFT and UPS is, at least in part, due to incomplete background subtraction of secondary electrons contributing to the UP spectra at high binding energies (negative relative to the Fermi level). The second point is that the shift in the energy of the filled portion of the total DOS tracks that of the d-band. Thus, in terms of its dependence on composition, the UPS-derived v-band energy serves a good proxy for the d-band energy.

3.3. H_2 – D_2 Exchange Activity on $\text{Cu}_x\text{Pd}_{1-x}$ CSAF. The H_2 – D_2 exchange activity of $\text{Cu}_x\text{Pd}_{1-x}$ alloys has been measured at 100 different compositions and reported as the conversion, $X(T; x, F)$, versus temperature, T , for various alloy compositions, x , and flow conditions, F . Once conditioned in the presence of H_2 , as described in section 2.3, the $\text{Cu}_x\text{Pd}_{1-x}$ CSAFs displayed stable activity during the course of the experiments. Conversion versus temperature curves, $X(T)$, for an inlet flow of 15 mL/min H_2 and 15 mL/min D_2 , are shown for several discrete alloy compositions in Figure 4a. For all alloy compositions, the conversion was $X = 0$ at $T = 333$ K but increased with increasing temperature. Figure 4b shows that the alloy became more active with decreasing Cu composition, x , and a maximum conversion of $X \approx 0.4$ was obtained at $x \approx 0.3$. These results are similar to those reported by O'Brien et al. over fixed beds of Cu, Pd, $\text{Pd}_{0.47}\text{Cu}_{0.53}$, and $\text{Pd}_{0.70}\text{Cu}_{0.30}$.⁴⁸

H_2 – D_2 exchange reactions were performed on the $\text{Cu}_x\text{Pd}_{1-x}$ CSAFs using three different inlet conditions—15 H_2 /15 D_2 , 25 H_2 /25 D_2 , and 15 H_2 /15 D_2 /30 Ar—where the numbers represent the total flow in mL/min to the 100 microreactors (Table 1). The effect of inlet flow conditions on the effluent HD flow rates for three different $\text{Cu}_x\text{Pd}_{1-x}$ alloy compositions can be seen in Figure 5. Changing the flow rates at a constant total $\text{H}_2 + \text{D}_2$ pressure of 1 atm has a minor effect on the conversion compared with reducing the $\text{H}_2 + \text{D}_2$ pressure to 0.5 atm.

4. DISCUSSION

4.1. Microkinetic Analysis of H_2 – D_2 Exchange on $\text{Cu}_x\text{Pd}_{1-x}$. Microkinetic analysis of H_2 – D_2 exchange on $\text{Cu}_x\text{Pd}_{1-x}$ was performed using the entire data set obtained

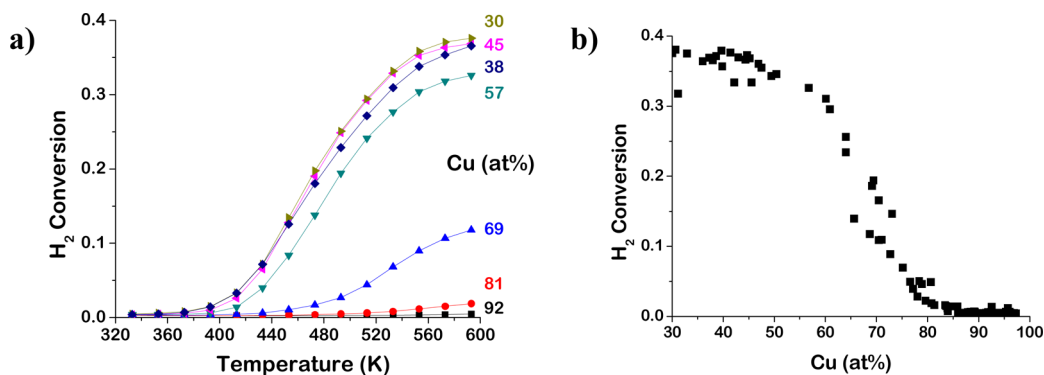


Figure 4. (a) H_2 – D_2 exchange conversion versus temperature on $\text{Cu}_x\text{Pd}_{1-x}$ alloys for several discrete Cu compositions, x . H_2 conversion increases with increasing T and decreasing x . (b) H_2 – D_2 exchange conversion versus Cu composition at $T = 593$ K. Inlet flow was 15 mL/min H_2 and 15 mL/min D_2 .

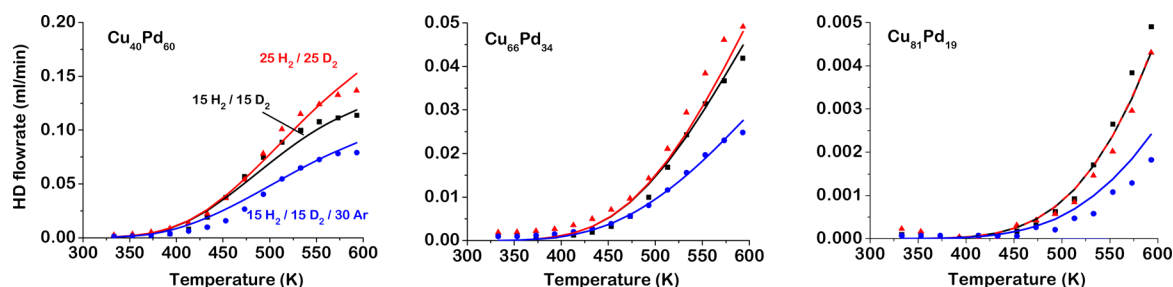
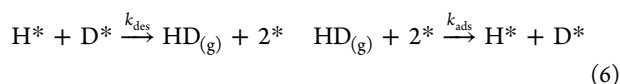
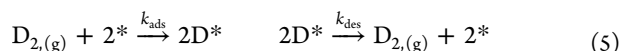
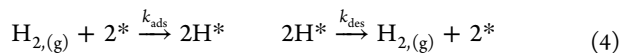


Figure 5. HD outlet flow rate versus temperature for three $\text{Cu}_x\text{Pd}_{1-x}$ alloy compositions ($x = 0.40, 0.66, 0.81$) and three inlet flow conditions. Data points are experimental measurements, and the solid lines are the fits of the microkinetic model to the data.

from the CSAF to estimate values of ν_{ads} , ν_{des} , $\Delta E_{\text{ads}}^\ddagger$, and $\Delta E_{\text{des}}^\ddagger$ as functions of alloy composition, x . The objective is to correlate these fundamental kinetic parameters with characteristics of the alloy's electronic structure. Kinetic analysis of the H_2 – D_2 exchange reaction was performed on the basis of the microkinetic model verified by O'Brien et al.⁴⁸ The model was based on a two-step, reversible reaction mechanism that occurred through dissociative adsorption and recombinative desorption of H_2 , D_2 , and HD requiring two sites, $*$, on the catalytic surface.



where the rate constants have Arrhenius form:

$$k_{\text{ads}} = \nu_{\text{ads}} \exp(-\Delta E_{\text{ads}}^\ddagger/RT) \\ k_{\text{des}} = \nu_{\text{des}} \exp(-\Delta E_{\text{des}}^\ddagger/RT) \quad (7)$$

In eq 7, ν_{ads} and ν_{des} are the pre-exponents and $\Delta E_{\text{ads}}^\ddagger$ and $\Delta E_{\text{des}}^\ddagger$ are the energy barriers for the dissociative adsorption and recombinative desorption steps, respectively. The gas constant is R , and T is temperature in K. In this model, kinetic isotope effects were neglected, that is, the rate constants k_{ads} and k_{des} were the same for steps 4, 5, and 6. In addition, ν_{ads} , ν_{des} , $\Delta E_{\text{ads}}^\ddagger$, and $\Delta E_{\text{des}}^\ddagger$ were assumed to be independent of the coverage of adsorbed species. O'Brien et al.⁴⁸ showed that through an integral mole balance on the microkinetic expression for the rate of formation of HD, an expression could be derived for the molar flow rate of HD in the outlet:

$$F_{\text{HD}}^{\text{out}} = F_{\text{H}_2}^{\text{in}} \left[1 - \exp \left(\frac{-k_{\text{ads}} P_{\text{tot}} A}{F_{\text{tot}} \left(1 + \sqrt{2 \frac{k_{\text{ads}} P_{\text{H}_2}^{\text{in}}}{k_{\text{des}}}} \right)^2} \right) \right] \quad (8)$$

where $F_{\text{HD}}^{\text{out}}$ and $F_{\text{H}_2}^{\text{in}}$ are the flow rates of HD in the effluent gas and H_2 in the feed gas, respectively. F_{tot} is the total molar flow rate of H_2 and D_2 at the inlet, and A is the surface area of the catalyst. P_{tot} and $P_{\text{H}_2}^{\text{in}}$ are the total pressure (H_2 and D_2) and the partial pressure of H_2 in the inlet, respectively. The conversion can be determined experimentally (eq 1) or from the microkinetic model (eq 8) using known reaction conditions and selected values of ν_{ads} , ν_{des} , $\Delta E_{\text{ads}}^\ddagger$, and $\Delta E_{\text{des}}^\ddagger$:

$$X_{\text{modl}} = \frac{F_{\text{HD}}^{\text{out}}}{2F_{\text{H}_2}^{\text{in}}} \quad (9)$$

To estimate the values of the kinetic parameters ν_{ads} , ν_{des} , $\Delta E_{\text{ads}}^\ddagger$, and $\Delta E_{\text{des}}^\ddagger$ for a given catalyst composition, x , the model prediction of conversion, X_{modl} , was fit to the measured conversions across all inlet flow conditions and temperatures simultaneously. The fit was performed by varying the four kinetic parameters to minimize the sum of the squared errors between the experimental and calculated conversions:

$$\text{SSE} = \sum_{i,j} [X_{\text{expt}}(F_i, T_j) - X_{\text{modl}}(F_i, T_j)]^2 \quad (10)$$

Optimization was performed in MATLAB using a “trust–region–reflective” algorithm that is based on an interior-reflective Newton method. Termination tolerance on the SSE function value was set to 10^{-10} . A central finite difference method was used to calculate gradients. Standard errors on optimized parameters were calculated using the MATLAB function *nlparci*. This function uses the residuals from the fit and the Jacobian matrix of the modeled conversions to calculate first the covariance matrix, then the standard errors.⁷⁵

The fidelity of the model can be judged by examining the plots of $F_{\text{HD}}^{\text{out}}(T)$ obtained from the model and the experimental data for the 300 different combinations of alloy composition and flow conditions. Examples are shown in Figure 5 for three alloys spanning a wide range of composition space. To better judge the overall model fidelity, the 4200 values of $F_{\text{HD}}^{\text{out}}$ measured experimentally and predicted by the model are compared as a parity plot in Figure 6.

4.2. Kinetic Parameters for H_2 – D_2 Exchange on $\text{Cu}_x\text{Pd}_{1-x}$. The primary goal of the work has been to use the data and the microkinetic model to estimate the values of ν_{ads} , ν_{des} , $\Delta E_{\text{ads}}^\ddagger$, and $\Delta E_{\text{des}}^\ddagger$ for each $\text{Cu}_x\text{Pd}_{1-x}$ alloy composition. Doing so represents by far the most comprehensive correlation of fundamental kinetic parameters with alloy catalyst composition achieved to date. Figure 7a plots $\log_{10}(\nu_{\text{ads}}(x))$, $\log_{10}(\nu_{\text{des}}(x))$ across $\text{Cu}_x\text{Pd}_{1-x}$ composition space for $x = 0.30$ to 0.97. The value of the pre-exponents for H_2 adsorption and desorption are $\log(\nu_{\text{ads}}) = -4.0 \pm 0.2 \text{ mol/m}^2/\text{s}/\text{Pa}$ and $\log(\nu_{\text{des}}) = 6.0 \pm 0.2 \text{ mol/m}^2/\text{s}$. Both are fairly independent of $\text{Cu}_x\text{Pd}_{1-x}$ alloy composition and in agreement with the predictions of transition state theory.⁷⁶ The model fit was first performed by optimizing all four parameters as described above within the composition range $x = 0.3$ – 0.8 . Having confirmed that the values of ν_{ads} and ν_{des} are independent of composition within this range, we subsequently performed the model fit by fixing pre-exponents to the values just mentioned and varying only $\Delta E_{\text{ads}}^\ddagger$ and $\Delta E_{\text{des}}^\ddagger$. These values of $\Delta E_{\text{ads}}^\ddagger$ are

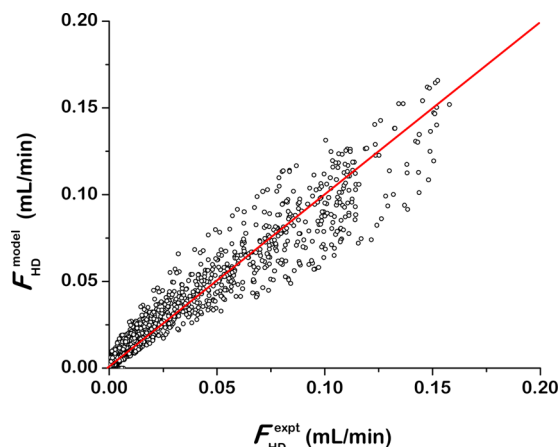


Figure 6. Parity plot of the HD flow rate predicted by the microkinetic model versus the HD flow rate measured experimentally. Data are shown for all 100 $\text{Cu}_x\text{Pd}_{1-x}$ alloy compositions ($x = 0.30\text{--}0.97$) at 14 temperatures ($T = 333\text{--}593$ K) and three inlet flow conditions (15 $\text{H}_2/15$ D_2 , 25 $\text{H}_2/25$, and 15 $\text{H}_2/15$ $\text{D}_2/30$ Ar).

plotted in Figure 7b. For $x < 0.6$, $\Delta E_{\text{ads}}^\ddagger \approx 0.15$ eV and is fairly independent of composition but then rises to $\Delta E_{\text{ads}}^\ddagger \approx 0.4$ eV for $x > 0.85$. Clearly, $\Delta E_{\text{ads}}^\ddagger(x)$ varies nonlinearly with $\text{Cu}_x\text{Pd}_{1-x}$ alloy composition. The value of $\Delta E_{\text{des}}^\ddagger$ rises from ~ 0.55 to ~ 0.65 eV over the composition range $x = 0.3\text{--}0.8$. O'Brien et al. measured the values of ν_{ads} , ν_{des} , $\Delta E_{\text{ads}}^\ddagger$, and $\Delta E_{\text{des}}^\ddagger$ for steady-state catalytic $\text{H}_2\text{--D}_2$ exchange over Cu, $\text{Pd}_{0.47}\text{Cu}_{0.53}$, $\text{Pd}_{0.70}\text{Cu}_{0.30}$, and Pd foil catalysts in a flow reactor.⁴⁸ The values reported in that study are plotted as open blue symbols in Figure 7b and are in overall agreement with the values measured over the $\text{Cu}_x\text{Pd}_{1-x}$ CSAF.

Cu–Pd alloys have an interesting phase diagram in the sense that, although Cu and Pd have FCC bulk structures, at $T < 900$ K, their alloy forms a B2 phase in the composition range around $\text{Cu}_{0.60}\text{Pd}_{0.40}$.⁵⁰ At $T > 900$ K, the Cu–Pd alloy exists as a FCC solid solution across the entire composition space. Priyadarshini et al. have demonstrated that a $\text{Cu}_x\text{Pd}_{1-x}$ CSAF annealed to 800 K exhibits the FCC to B2 to FCC phase transitions over the composition range $0.5 < x < 0.7$.¹¹ One feature of the $\text{H}_2\text{--D}_2$ exchange measurements reported by O'Brien et al. is that it was possible to measure the reaction kinetics over $\text{Cu}_{0.53}\text{Pd}_{0.47}$ in both its FCC and B2 phases.⁴⁸ Interestingly, the FCC phase was much more active than the B2 phase. Microkinetic modeling yielded values of $\Delta E_{\text{ads}}^\ddagger(x) = 0.15$

± 0.02 eV for the B2 phase and $\Delta E_{\text{ads}}^\ddagger(x) = 0.00 \pm 0.02$ eV for the more active FCC phase. Results for the $\text{Cu}_x\text{Pd}_{1-x}$ CSAF near $x = 0.53$ reported in Figure 7 are consistent with the $\text{H}_2\text{--D}_2$ exchange reaction on the CSAF occurring over the B2 phase, the most stable phase at the reaction temperatures, $T < 600$ K. This indicates that under catalytic conditions, the alloy retains its thermodynamically preferred bulk structure.

Over the composition range $x < 0.7$, $\Delta E_{\text{ads}}^\ddagger(x) \ll \Delta E_{\text{des}}^\ddagger(x)$, which suggests that the $\text{H}_2\text{--D}_2$ exchange reaction is rate-limited by the recombinative desorption of HD. This is entirely consistent with the results of O'Brien et al. for $\text{H}_2\text{--D}_2$ exchange over the $\text{Pd}_{0.47}\text{Cu}_{0.53}$, $\text{Pd}_{0.70}\text{Cu}_{0.30}$, and Pd foil catalysts.⁴⁸ In that study, the reaction rate over these foils was found to be independent of total H_2/D_2 pressure, implying that the surface was saturated with $\text{H}_{(\text{ad})}$ and $\text{D}_{(\text{ad})}$, consistent with a desorption-limited process. In contrast, O'Brien et al. observed that the reaction rate over the pure Cu foil was sensitive to the total H_2/D_2 pressure, implying that the reaction rate was limited by dissociative adsorption of H_2 and D_2 . Another indicator of adsorption rate limitation over Cu was that microkinetic modeling of the $\text{H}_2\text{--D}_2$ exchange kinetics yielded a large uncertainty in $\Delta E_{\text{des}}^\ddagger$ that was greater than the magnitude of $\Delta E_{\text{des}}^\ddagger$ itself, $\sigma E_{\text{des}}^\ddagger > \Delta E_{\text{des}}^\ddagger$. In other words, the $\text{H}_2\text{--D}_2$ exchange kinetics over Cu are insensitive to the value of $\Delta E_{\text{des}}^\ddagger$ because the reaction is rate-limited by dissociative adsorption. Similarly, over the $\text{Cu}_x\text{Pd}_{1-x}$ CSAF we observe that $\sigma E_{\text{des}}^\ddagger > \Delta E_{\text{des}}^\ddagger$ for $x > 0.8$, and therefore, we do not report the values of $\Delta E_{\text{des}}^\ddagger$ for $x > 0.8$ in Figure 7b. The fact that $\sigma E_{\text{des}}^\ddagger > \Delta E_{\text{des}}^\ddagger$ for $x > 0.8$ suggests that at a composition of $x \approx 0.8$, there is a switch in the rate-limiting step from recombinative desorption of HD ($x < 0.8$) to dissociative adsorption of H_2/D_2 ($x > 0.8$).

4.3. Correlation of Activity and Structure Across Composition Space. The overarching goal of this work has been to correlate fundamental kinetic parameters for catalytic $\text{H}_2\text{--D}_2$ exchange over $\text{Cu}_x\text{Pd}_{1-x}$ alloys with characteristics of their electronic structure. The strategy has been to mimic experimentally the approach of DFT studies of various catalytic processes^{5–8,51,77} that correlate the calculated mean energy of the d-band, ε_{d} , of various metals with the calculated barriers, ΔE^\ddagger , to elementary reactions steps on their surfaces.^{5–8,51,77} In the work described above, we have used UP spectra from a $\text{Cu}_x\text{Pd}_{1-x}$ CSAF to measure the energy of the filled valence band center, $\varepsilon_{\text{v}}(x)$, and to obtain $\Delta E_{\text{ads}}^\ddagger(x)$ and $\Delta E_{\text{des}}^\ddagger(x)$ from $\text{H}_2\text{--D}_2$ exchange kinetics. Figure 8 plots the resulting $\Delta E_{\text{ads}}^\ddagger(\varepsilon_{\text{v}})$ and $\Delta E_{\text{des}}^\ddagger(\varepsilon_{\text{v}})$ obtained at 100 different $\text{Cu}_x\text{Pd}_{1-x}$ alloy

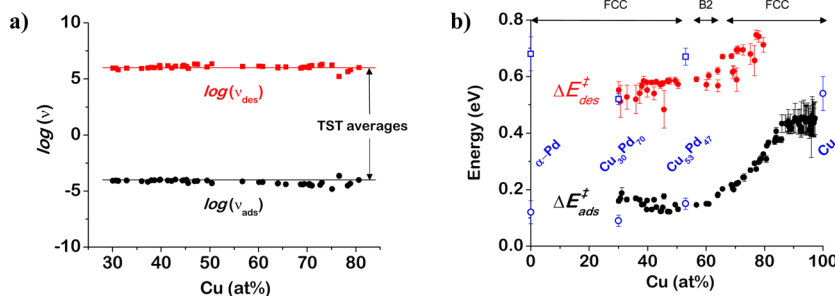


Figure 7. (a) Measured pre-exponents for dissociative adsorption of H_2 , $\nu_{\text{ads}}(x)$ (●), and recombinative desorption of H_2 , $\nu_{\text{des}}(x)$ (red solid square) on $\text{Cu}_x\text{Pd}_{1-x}$. Black and red lines represent transition state theory estimates of the pre-exponents for these reaction steps. (b) Measured activation barriers for dissociative adsorption, $\Delta E_{\text{ads}}^\ddagger(x)$ (●), and recombinative desorption, $\Delta E_{\text{des}}^\ddagger(x)$ (red solid square) of H_2 versus $\text{Cu}_x\text{Pd}_{1-x}$ composition. Open symbols (blue circle and blue box) are the activation barriers estimated from $\text{H}_2\text{--D}_2$ exchange kinetics measured over fixed beds of single composition foil catalysts.

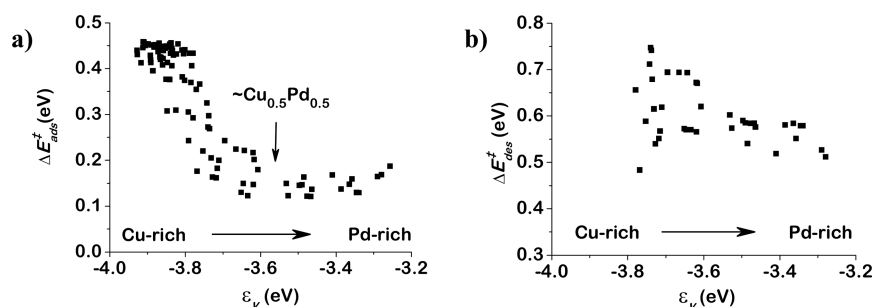


Figure 8. Energy barriers for (a) dissociative adsorption of H_2 , $\Delta E_{\text{ads}}^{\ddagger}(x)$, and (b) recombinative desorption of H_2 , $\Delta E_{\text{des}}^{\ddagger}(x)$, plotted versus the energy of the v-band center, $\epsilon_v(x)$, measured on 100 $\text{Cu}_x\text{Pd}_{1-x}$ compositions.

compositions. The overall correlation shows that as ϵ_v shifts toward the Fermi level, $\Delta E_{\text{ads}}^{\ddagger}(\epsilon_v)$ and $\Delta E_{\text{des}}^{\ddagger}(\epsilon_v)$ decrease, as suggested from DFT studies.^{5,8,78–82}

The plot of $\Delta E_{\text{ads}}^{\ddagger}(\epsilon_v)$ in Figure 8a reveals a decrease in the H_2 adsorption barrier with increasing ϵ_v , but the trend is not linear across the entire $\text{Cu}_x\text{Pd}_{1-x}$ composition space. The value of $\Delta E_{\text{ads}}^{\ddagger}(\epsilon_v)$ decreases at a rate of ~ 1.5 eV/eV over the range from pure Cu to $\sim\text{Cu}_{0.5}\text{Pd}_{0.5}$ but then remains constant to $\text{Cu}_{0.3}\text{Pd}_{0.7}$. To put the value of 1.5 eV/eV in perspective, a DFT study of the reaction energy (not barrier) for dissociative adsorption of H_2 , $\Delta E_{\text{ads}}^{\text{H}_2}$, on seven Pt alloys found a change of ~ 1.7 eV per eV shift in ϵ_d of those alloys.⁸³ By comparison with $\Delta E_{\text{ads}}^{\ddagger}(\epsilon_v)$ on $\text{Cu}_x\text{Pd}_{1-x}$, $\Delta E_{\text{des}}^{\ddagger}$ is much less sensitive to ϵ_v , dropping at ~ 0.2 eV/eV (Figure 8b). However, the correlation for $\Delta E_{\text{des}}^{\ddagger}(\epsilon_v)$ is significantly poorer than that of $\Delta E_{\text{ads}}^{\ddagger}(\epsilon_v)$, largely because the measured values of $\Delta E_{\text{des}}^{\ddagger}$ span a much narrower range and have been measured over a narrower range of $\text{Cu}_x\text{Pd}_{1-x}$ compositions.

The positions of the v-bands derived from the UP spectra (Figure 3) exhibit a roughly linear dependence on $\text{Cu}_x\text{Pd}_{1-x}$ composition, with the obvious exception of some scatter in the range $x = 0.37–0.5$. In contrast, $\Delta E_{\text{ads}}^{\ddagger}(\epsilon_v)$ exhibits behavior that is nonlinear. This suggests that there are processes occurring on the $\text{Cu}_x\text{Pd}_{1-x}$ CSAF that are not captured in models of surface reactions in which DFT predicts a linear response of reaction energetics to ϵ_v . One process that is not captured in most DFT studies of alloy surface chemistry is segregation. Although segregation in alloys is known to be ubiquitous, it introduces a high level of configurational complexity into atomistic simulations of process on alloy surfaces.^{84–89} Segregation at clean CuPd alloy surfaces studied under ultrahigh vacuum is known to result in an excess of Cu in the topmost surface layer.^{11,90–93} A low-energy ion scattering study on a $\text{Cu}_x\text{Pd}_{1-x}$ CSAF observed Cu segregation across all of composition space.¹¹ To complicate matters further, segregation is known to be sensitive to the presence of adsorbed species. For example, in the case of sulfur adsorbed on a $\text{Cu}_x\text{Pd}_{1-x}$ CSAF, the heat of Cu segregation is reversed from being exothermic to endothermic.⁹⁴ Although we cannot address the problem of segregation under reaction conditions directly, the possibility that surface segregation is responsible for the nonlinear behavior of $\Delta E_{\text{ads}}^{\ddagger}(\epsilon_v)$ is quite possible and worth addressing.

Under conditions of $\text{H}_2–\text{D}_2$ exchange at 1 atm, the CuPd alloy surfaces are modified by the presence of atomic hydrogen; however, direct study of surface segregation under reaction conditions is nontrivial and has not been attempted. The prior work of O'Brien et al. used the results of microkinetic modeling on Cu, Pd, and various CuPd foil catalysts to estimate indirectly the coverage of hydrogen under conditions of steady state $\text{H}_2–$

D_2 exchange.⁴⁸ Estimates based on that work are that on the $\text{Cu}_x\text{Pd}_{1-x}$ catalysts with $x = 0, 0.30$, and 0.53 , the total H and D coverage varies from ~ 0.9 to ~ 0.2 ML as the temperature increases from 300 to 600 K. On the pure Cu catalyst, the hydrogen coverage was estimated to be $\sim 10\%$ across the entire temperature range. This, of course, complicates the segregation problem because the hydrogen coverage depends on both $\text{Cu}_x\text{Pd}_{1-x}$ composition and temperature. Hydrogen-induced segregation on CuPd alloys is the result of a competition between segregation to the clean surface and the differential heat of adsorption of hydrogen on Cu and Pd. A prior ion scattering study of segregation at the clean surface of a $\text{Cu}_x\text{Pd}_{1-x}$ CSAF has shown that Cu segregation occurs preferentially (exothermic) at all compositions and that the heat of segregation varies from -0.05 eV on the Pd-rich alloys to 0 eV on the Cu-rich alloys.¹¹

The adsorption energy of hydrogen, $\Delta E_{\text{ads}}^{\text{H}_2}$, is calculated to be higher on Pd (-0.62 eV/H) than on Cu (-0.19 eV/H)⁹⁵ and the difference is greater than the segregation energy of Cu at the $\text{Cu}_x\text{Pd}_{1-x}$ surface. More important than the hydrogen adsorption energies on the pure components are the hydrogen adsorption energies on the alloys. These can be estimated from the differences in the barriers to hydrogen desorption and adsorption plotted in Figure 7b, $\Delta E_{\text{ads}}^{\text{H}_2} = \Delta E_{\text{des}}^{\ddagger} - \Delta E_{\text{ads}}^{\ddagger}$. The hydrogen adsorption energy varies from $\Delta E_{\text{ads}}^{\text{H}_2} \cong 0.55$ eV at $x = 0.3$ to $\Delta E_{\text{ads}}^{\text{H}_2} \cong 0.35$ eV at $x = 0.8$ and is much greater than the Cu segregation energy across the entire range. As a consequence, the adsorption of hydrogen on CuPd alloys is expected to favor the segregation of Pd at all alloy compositions. This problem has been dealt with by DFT modeling in a companion paper to this current investigation. That study quantifies the extent of hydrogen induced Pd segregation on the $\text{Cu}_x\text{Pd}_{1-x}$ surfaces and its impact on the energetics of H_2 adsorption.⁹⁶

One hypothesis for the nonlinear behavior of the $\Delta E_{\text{ads}}^{\ddagger}(\epsilon_v)$ observed on the $\text{Cu}_x\text{Pd}_{1-x}$ CSAF is that hydrogen-induced segregation is causing changes in the surface composition of the alloy. If the surface concentration of Pd approaches saturation in the Pd-rich alloy composition range, then the measured value of $\Delta E_{\text{ads}}^{\ddagger}$ would be independent of composition, as observed for $x < 0.6$ in Figure 7b and independent of the v-band energy for $\epsilon_v > -3.6$ eV, as observed in Figure 8a. It is important to point out that if the topmost layer of the alloy is saturated in Pd, as a result of hydrogen-induced segregation, the value of $\Delta E_{\text{ads}}^{\ddagger}$ ceases to depend on the bulk alloy composition because the surface composition is primarily Pd and no longer changing with bulk composition. This is equivalent to saying that the electronic structure of the topmost layer is also independent of bulk alloy composition. Note that the value of the v-band

energy measured using UPS reflects the electronic structure of the near surface rather than the topmost surface layer. The escape depth or mean free paths of UV photoelectrons with kinetic energies of 10–15 eV fall in the range 5–15 Å, corresponding to 2–5 atomic layers of the metal.⁹⁷ Modeling of this problem and the effects of surface segregation on alloy reactivity is complicated by the issue of segregation and the need to account for surfaces with numerous atomic configurations, compounded by the need to account for adsorbate induced segregation. These ideas are quantified in a companion paper to this work.⁹⁶

4.4. Correlation of alloy properties and catalysis. The goal of the work presented herein has been the demonstration of a methodology for correlating the fundamental kinetic parameters for reactions on catalytic alloys with their surface properties across large continuous regions of alloy composition space. Using the CSAFs and the multichannel microreactor array,^{12,37,53} these correlations can be established much more rapidly than by traditional studies of catalysts with discrete composition. Furthermore, the methodology is quite general as CSAFs are readily prepared from almost all combinations of elementary components and are readily characterized across composition space using any surface analysis method capable of spatial resolution on the order of a few hundred microns.

The greatest constraints on the applicability of the methodology described herein arise from the types of catalytic reactions amenable to study. In its current form, the microchannel reactor array can be used to study the kinetics of catalytic gas–solid reactions that have turnovers of $>10^{-5} \text{ s}^{-1}$ (given a good mass spectrometer) at temperatures $<600 \text{ K}$ and pressures $<1 \text{ atm}$.³⁷ It is suitable only for study of those types of reactions that are amenable to product analysis using mass spectrometry, which is not a serious limitation. More importantly, one must be able to extract fundamental reaction parameters such as kinetics barriers and pre-exponential factors from kinetic data obtained over a range of temperatures and reactant partial pressures. This implies that the surface reaction mechanism is known and that it is not too complex for analysis by realistic microkinetic modeling.

5. CONCLUSION

The use of CSAFs as libraries of alloy composition, coupled with surface analysis and measurements of catalytic reaction kinetics allows study of otherwise intractable problems in alloy catalysis. The methodology developed in this work is ideally suited to mapping and understanding fundamental properties of alloy catalysts across their composition space. By mapping surface electronic structure, as characterized by the energy of the d-band, and measuring the barriers to elementary reactions steps, as determined from microkinetic modeling, both as functions of alloy composition, one can construct correlations between the two. The measured correlation $\Delta E_{\text{ads}}^{\ddagger}(\epsilon_v)$ for H_2 on $\text{Cu}_x\text{Pd}_{1-x}$ alloys demonstrates that the reaction barrier decreases nonlinearly with the shift of ϵ_v toward the Fermi level. Over the range $\epsilon_v = -3.95$ to -3.65 eV the value of $\Delta E_{\text{ads}}^{\ddagger}$ decreases linearly as predicted by DFT studies for many surface reactions. Over the range $\epsilon_v = -3.65$ to -3.35 eV the value of $\Delta E_{\text{ads}}^{\ddagger}$ is constant. We suggest that this behavior reflects hydrogen induced surface segregation of Pd such that the surfaces of the Pd-rich alloys with ϵ_v closest to the Fermi level are saturated in Pd. Because $\Delta E_{\text{ads}}^{\ddagger}$ is sensitive to surface composition only, while the measured values of ϵ_v depend on bulk alloy composition, $\Delta E_{\text{ads}}^{\ddagger}$ becomes insensitive to ϵ_v when

the bulk alloy composition is high enough in Pd to result in the surface layer being saturated with Pd due to hydrogen-induced segregation.

■ ASSOCIATED CONTENT

Supporting Information

The following file is available free of charge on the ACS Publications website at DOI: 10.1021/cs501586t.

Detailed information about each of the bulk structures used in this study ([PDF](#))

■ AUTHOR INFORMATION

Corresponding Author

*Phone: 412-268-3848. E-mail: gellman@cmu.edu.

Notes

The authors declare no competing financial interest.

■ ACKNOWLEDGMENTS

As part of the National Energy Technology Laboratory's Regional University Alliance (NETL-RUA), a collaborative initiative of the NETL, this technical effort was performed under the RES Contract DE-FE0004000. J.R.K. gratefully acknowledges partial support from the DOE Office of Science Early Career Research program (DE-SC0004031). JBM gratefully acknowledges partial support from the National Science Foundation (CBET 1033804).

■ REFERENCES

- (1) Juszczyk, W.; Karpinski, Z.; Lomot, D.; Pielaszek, J.; Sobczak, J. *W. J. Catal.* **1995**, *151*, 67–76.
- (2) Baber, A. E.; Tierney, H. L.; Sykes, E. C. H. *ACS Nano* **2010**, *4*, 1637–1645.
- (3) Hammer, B.; Norskov, J. K. *Nature* **1995**, *376*, 238–240.
- (4) Wei, T.; Wang, J.; Goodman, D. W. *J. Phys. Chem. C* **2007**, *111*, 8781–8788.
- (5) Hammer, B.; Norskov, J. K. *Adv. Catal.* **2000**, *45*, 71–129.
- (6) Ruban, A.; Hammer, B.; Stoltze, P.; Skriver, H. L.; Norskov, J. K. *J. Mol. Catal. A: Chem.* **1997**, *115*, 421–429.
- (7) Sheth, P. A.; Neurock, M.; Smith, C. M. *J. Phys. Chem. B* **2005**, *109*, 12449–12466.
- (8) Hammer, B.; Morikawa, Y.; Norskov, J. K. *Phys. Rev. Lett.* **1996**, *76*, 2141–2144.
- (9) Mavrikakis, M.; Hammer, B.; Norskov, J. K. *Phys. Rev. Lett.* **1998**, *81*, 2819–2822.
- (10) Yi, C. W.; Luo, K.; Wei, T.; Goodman, D. W. *J. Phys. Chem. B* **2005**, *109*, 18535–18540.
- (11) Priyadarshini, D.; Kondratyuk, P.; Picard, Y. N.; Morreale, B. D.; Gellman, A. J.; Miller, J. B. *J. Phys. Chem. C* **2011**, *115*, 10155–10163.
- (12) Fleutot, B.; Miller, J. B.; Gellman, A. J. *Vac. Sci. Technol. A* **2012**, *30*, 061511.
- (13) Boettcher, A.; Haase, G.; Thun, R. *Zeitschrift Metallkunde* **1955**, *46*, 386–400.
- (14) Hanak, J. J. *J. Mater. Sci.* **1970**, *5*, 964.
- (15) Rar, A.; Frafjord, J. J.; Fowlkes, J. D.; Specht, E. D.; Rack, P. D.; Santella, M. L.; Bei, H.; George, E. P.; Pharr, G. M. *Meas. Sci. Technol.* **2005**, *16*, 46–53.
- (16) Ohkubo, I.; Christen, H. M.; Khalifah, P.; Sathyamurthy, S.; Zhai, H. Y.; Rouleau, C. M.; Mandrus, D. G.; Lowndes, D. H. *Appl. Surf. Sci.* **2004**, *223*, 35–38.
- (17) Woo, N. C.; Ng, B. G.; van Dover, R. B. *Rev. Sci. Instrum.* **2007**, *78*, -.
- (18) Cooper, J. S.; McGinn, P. J. *Appl. Surf. Sci.* **2007**, *254*, 662–668.
- (19) van Dover, R. B.; Schneemeyer, L. F. *Macromol. Rapid Commun.* **2004**, *25*, 150–157.
- (20) Guerin, S.; Hayden, B. E. *J. Comb. Chem.* **2005**, *8*, 66–73.

- (21) Yamada, Y.; Fukumura, T.; Ikeda, M.; Ohtani, M.; Toyosaki, H.; Ohtomo, A.; Matsukura, F.; Ohno, H.; Kawasaki, M. *J. Supercond.* **2005**, *18*, 109–113.
- (22) Dell'Anna, R.; Lazzeri, P.; Canteri, R.; Long, C. J.; Hattribk-Simpers, J.; Takeuchi, I.; Anderle, M. *QSAR Comb. Sci.* **2008**, *27*, 171–178.
- (23) Kennedy, K.; Stefansky, T.; Davy, G.; Zackay, V. F.; Parker, E. R. *J. Appl. Phys.* **1965**, *36*, 3808–3810.
- (24) Takeuchi, I.; Famodu, O. O.; Read, J. C.; Aronova, M. A.; Chang, K. S.; Craciunescu, C.; Lofland, S. E.; Wuttig, M.; Wellstood, F. C.; Knauss, L.; Orozco, A. *Nat. Mater.* **2003**, *2*, 180–184.
- (25) Hasegawa, K.; Ahmet, P.; Okazaki, N.; Hasegawa, T.; Fujimoto, K.; Watanabe, M.; Chikyow, T.; Koinuma, H. *Appl. Surf. Sci.* **2004**, *223*, 229–232.
- (26) Chang, H.; Takeuchi, I.; Xiang, X.-D. *Appl. Phys. Lett.* **1999**, *74*, 1165–1167.
- (27) Wang, J.; Yoo, Y.; Gao, C.; Takeuchi, I.; Sun, X.; Chang, H.; Xiang, X.-D.; Schultz, P. G. *Science* **1998**, *279*, 1712–1714.
- (28) Koinuma, H.; Takeuchi, I. *Nat. Mater.* **2004**, *3*, 429–438.
- (29) Farrusseng, D. *Surf. Sci. Rep.* **2008**, *63*, 487–513.
- (30) Pérez-Ramírez, J.; Berger, R. J.; Mul, G.; Kapteijn, F.; Moulijn, J. A. *Catal. Today* **2000**, *60*, 93–109.
- (31) Morra, G.; Desmartin-Chomel, A.; Daniel, C.; Ravon, U.; Farrusseng, D.; Cowan, R.; Krusche, M.; Mirodatos, C. *Chem. Eng. J.* **2008**, *138*, 379–388.
- (32) Senkan, S.; Krantz, K.; Ozturk, S.; Zengin, V.; Onal, I. *Angew. Chem., Int. Ed.* **1999**, *38*, 2794–2799.
- (33) Guerin, S.; Hayden, B. E.; Smith, D. C. *J. Comb. Chem.* **2007**, *10*, 37–43.
- (34) Gremaud, R.; Broedersz, C. P.; Borgschulte, A.; van Setten, M. J.; Schreuders, H.; Slaman, M.; Dam, B.; Griessen, R. *Acta Mater.* **2010**, *58*, 658–668.
- (35) Al-Odail, F. A.; Anastasopoulos, A.; Hayden, B. E. *Phys. Chem. Chem. Phys.* **2010**, *12*, 11398–11406.
- (36) Anastasopoulos, A.; Hannah, L.; Hayden, B. E. *J. Catal.* **2013**, *305*, 27–35.
- (37) Kondratyuk, P.; Gumuslu, G.; Shukla, S.; Miller, J. B.; Morreale, B. D.; Gellman, A. J. *J. Catal.* **2013**, *300*, 55–62.
- (38) Adhikari, S.; Fernando, S. *Ind. Eng. Chem. Res.* **2006**, *45*, 875–881.
- (39) Morreale, B. D., et al. In *Inorganic Membranes for Energy and Environmental Applications*; Bose, A. C., Ed.; Springer: New York, 2009.
- (40) Lanning, B. R., et al. In *Inorganic Membranes for Energy and Environmental Applications*; Bose, A. C., Ed.; Springer: New York, 2009.
- (41) Roa, F.; Way, J. D.; McCormick, R. L.; Paglieri, S. N. *Chem. Eng. J.* **2003**, *93*, 11–22.
- (42) Piper, J. *J. Appl. Phys.* **1966**, *37*, 715–8.
- (43) Knapton, A. *Platinum Met. Rev.* **1977**, *21*, 44.
- (44) Horiuti, J.; Miyahara, K. *National Bureau of Standards*; U.S. Government Printing Office: Washington, DC, 1967.
- (45) Bond, G.; Philipson, J.; Wells, P.; Winterbottom, J. *Trans. Faraday Soc.* **1966**, *62*, 443–454.
- (46) Khan, N. A.; Shaikhutdinov, S.; Freund, H. J. *Catal. Lett.* **2006**, *108*, 159–164.
- (47) Stacchiola, D.; Tysøe, W. T. *Surf. Sci.* **2003**, *540*, L600–L604.
- (48) O'Brien, C. P.; Miller, J. B.; Morreale, B. D.; Gellman, A. J. *J. Phys. Chem. C* **2011**, *115*, 24221–24230.
- (49) Johansson, M.; Skúlason, E.; Nielsen, G.; Murphy, S.; Nielsen, R. M.; Chorkendorff, I. *Surf. Sci.* **2010**, *604*, 718–729.
- (50) Subramanian, P. R.; Laughlin, D. E. *J. Phase Equilib.* **1991**, *12*, 231–243.
- (51) Hammer, B.; Nørskov, J. K. *Surf. Sci.* **1995**, *343*, 211–220.
- (52) Pallassana, V.; Neurock, M.; Hansen, L. B.; Hammer, B.; Nørskov, J. K. *Phys. Rev. B: Condens. Matter Mater. Phys.* **1999**, *60*, 6146–6154.
- (53) Priyadarshini, D.; Kondratyuk, P.; Miller, J. B.; Gellman, A. J. *J. Vac. Sci. Technol. A* **2012**, *30*(10), 1116/1.3664078.
- (54) He, J. W.; Shea, W. L.; Jiang, X.; Goodman, D. W. *J. Vac. Sci. Technol. A* **1990**, *8*, 2435–2444.
- (55) Park, C.; Bauer, E.; Poppa, H. *Surf. Sci.* **1985**, *154*, 371–393.
- (56) McQuarrie, D. A. *Statistical Mechanics*; University Science Books: Sausalito, CA, 2000.
- (57) Bärthlein, S.; Winning, E.; Hart, G. L. W.; Müller, S. *Acta Mater.* **2009**, *57*, 1660–1665.
- (58) Lu, Z. W.; Wei, S. H.; Zunger, A.; Frota-Pessoa, S.; Ferreira, L. G. *Phys. Rev. B: Condens. Matter Mater. Phys.* **1991**, *44*, 512–544.
- (59) Kresse, G.; Furthmüller, J. *Comput. Mater. Sci.* **1996**, *6*, 15–50.
- (60) Kresse, G.; Furthmüller, J. *Phys. Rev. B: Condens. Matter Mater. Phys.* **1996**, *54*, 11169–11186.
- (61) Perdew, J. P.; Burke, K.; Ernzerhof, M. *Phys. Rev. Lett.* **1997**, *78*, 1396–1396.
- (62) Perdew, J. P.; Burke, K.; Ernzerhof, M. *Phys. Rev. Lett.* **1996**, *77*, 3865–3868.
- (63) Blochl, P. E. *Phys. Rev. B: Condens. Matter Mater. Phys.* **1994**, *50*, 17953–17979.
- (64) Kresse, G.; Joubert, D. *Phys. Rev. B: Condens. Matter Mater. Phys.* **1999**, *59*, 1758–1775.
- (65) Monkhorst, H. J.; Pack, J. D. *Phys. Rev. B* **1976**, *13*, 5188–5192.
- (66) Fleutot, B.; Miller, J. B.; Gellman, A. J. *J. Vac. Sci. Technol., A* **2012**, *30*, -.
- (67) Li, X. M.; Zhang, Z. M.; Henrich, V. E. *J. Electron Spectrosc. Relat. Phenom.* **1993**, *63*, 253–265.
- (68) Mun, B. S.; Watanabe, M.; Rossi, M.; Stamenkovic, V.; Markovic, N. M.; Ross, P. N., Jr. *J. Chem. Phys.* **2005**, *123*, 204717–204717.
- (69) Eastman, D. E.; Grobman, W. D. *Phys. Rev. Lett.* **1973**, *30*, 177–180.
- (70) Alfonso, D. R.; Cugini, A. V.; Sholl, D. S. *Surf. Sci.* **2003**, *546*, 12–26.
- (71) Kratzer, P.; Hammer, B.; Nørskov, J. K. *Surf. Sci.* **1996**, *359*, 45–53.
- (72) Eichler, A.; Mittendorfer, F.; Hafner, J. *Phys. Rev. B: Condens. Matter Mater. Phys.* **2000**, *62*, 4744–4755.
- (73) Lopez, N.; Nørskov, J. K. *Surf. Sci.* **2001**, *477*, 59–75.
- (74) Inoglu, N.; Kitchin, J. R. *Mol. Simul.* **2010**, *36*, 633–638.
- (75) Bates, D. M.; Watts, D. G. In *Nonlinear Regression Analysis and Its Applications*; John Wiley & Sons, Inc.: New York, 2008; pp 32–66.
- (76) Dumesic, J. A. *The Microkinetics of Heterogeneous Catalysis*; American Chemical Society: Washington, DC, 1993.
- (77) Eichler, A.; Kresse, G.; Hafner, J. *Surf. Sci.* **1998**, *397*, 116–136.
- (78) Zhang, J. L.; Vukmirovic, M. B.; Xu, Y.; Mavrikakis, M.; Adzic, R. R. *Angew. Chem., Int. Ed.* **2005**, *44*, 2132–2135.
- (79) Greeley, J.; Mavrikakis, M. *Nat. Mater.* **2004**, *3*, 810–815.
- (80) Xu, Y.; Ruban, A. V.; Mavrikakis, M. *J. Am. Chem. Soc.* **2004**, *126*, 4717–4725.
- (81) Rodriguez, J. A.; Goodman, D. W. *Science* **1992**, *257*, 897–903.
- (82) Christoffersen, E.; Liu, P.; Ruban, A.; Skriver, H. L.; Nørskov, J. K. *J. Catal.* **2001**, *199*, 123–131.
- (83) Kitchin, J.; Nørskov, J. K.; Barteau, M.; Chen, J. *J. Chem. Phys.* **2004**, *120*, 10240–10246.
- (84) Polak, M.; Rubanovich, L. *Surf. Sci. Rep.* **2000**, *38*, 127–194.
- (85) Newton, M. A.; Francis, S. M.; Bowker, M. *Surf. Sci.* **1991**, *259*, 56–64.
- (86) Abraham, F. F.; Brundle, C. R. *J. Vac. Sci. Technol.* **1981**, *18*, 506–519.
- (87) Rittner, J. D.; Foiles, S. M.; Seidman, D. N. *Phys. Rev. B: Condens. Matter Mater. Phys.* **1994**, *50*, 12004–12014.
- (88) Wynblatt, P.; Landa, A. *Comput. Mater. Sci.* **1999**, *15*, 250–263.
- (89) Deng, H.; Hu, W.; Shu, X.; Zhang, B. *Appl. Surf. Sci.* **2004**, *221*, 408–414.
- (90) Miller, J. B.; Matranga, C.; Gellman, A. J. *Surf. Sci.* **2008**, *602*, 375–382.
- (91) Newton, M. A.; Francis, S. M.; Li, Y.; Law, D.; Bowker, M. *Surf. Sci.* **1991**, *259*, 45–55.
- (92) Bergmans, R. H.; van de Grift, M.; van der Gon, A. W. D.; Brongersma, H. H. *Surf. Sci.* **1996**, *345*, 303–312.

- (93) Mousa, M. S.; Loboda-Cackovic, J.; Block, J. H. *Vacuum* **1995**, *46*, 117–125.
- (94) Miller, J. B.; Priyadarshini, D.; Gellman, A. J. *Surf. Sci.* **2012**, *606*, 1520–1526.
- (95) Ferrin, P.; Kandoi, S.; Nilekar, A. U.; Mavrikakis, M. *Surf. Sci.* **2012**, *606*, 679–689.
- (96) Boes, J.; Gumuslu, G.; Miller, J.; Gellman, A.; Kitchin, J. *ACS Catal.* **2015**, *5*, 1020–1026.
- (97) Seah, M. P.; Dench, W. A. *Surf. Interface Anal.* **1979**, *1*, 2–11.